

AGN-driven helium reionization and the incidence of extended He III regions at redshift $z > 3$

Michele Compostella^{1*}, Sebastiano Cantalupo^{2*} and Cristiano Porciani^{1*}

¹*Argelander Institut für Astronomie der Universität Bonn, Auf dem Hügel 71, Bonn, D-53121, DE.*

²*Department of Astronomy and Astrophysics, UCO/Lick Observatory, University of California, 1156 High Street, Santa Cruz, CA 95064, USA.*

Accepted ; Received ; in original form .

ABSTRACT

We use hydrodynamic simulations post-processed with the radiative-transfer code RADAMESH to assess recent claims that the low He II opacity observed in $z > 3$ quasar spectra may be incompatible with models of He II reionization driven by the observed population of active galactic nuclei (AGNs). In particular, building upon our previous work, we consider an early population of sources and start the radiative-transfer calculation at redshifts $z \geq 5$. Our model faithfully reproduces the emissivity of optically selected AGNs as inferred from measurements of their luminosity function. We find that He II reionization is very extended in redshift ($\Delta z \geq 2$) and highly spatially inhomogeneous. In fact, mock spectra extracted from the simulations show a large variability in the evolution of the He II effective optical depth within chunks of size $\Delta z = 0.04$. Regions with low opacity ($\tau_{\text{He II}}^{\text{eff}} < 3$) can be found at high redshift, in agreement with the most recent observations of UV-transmitting quasars. At the highest redshift currently probed by observations ($z \sim 3.4$), our updated model predicts a much lower He II effective optical depth than previous simulations in the literature relieving most of the tension with the current data, that, however, still persists at about the (Gaussian) 1σ to 2σ level. Given the very small number of observed lines of sight, our analysis indicates that current data cannot rule out a purely AGN-driven scenario with high statistical significance.

Key words: radiative transfer – intergalactic medium – quasars: general – cosmology: theory – large-scale structure of the Universe.

1 INTRODUCTION

The first few Gyr of cosmic history witnessed at least two major changes in the main constituents of the intergalactic medium (IGM). The ionized fraction of hydrogen and helium dramatically increased in a relatively short time-scale passing from nearly fully neutral to fully ionized (see Fan et al. 2006a; Meiksin 2009, for a detailed review). The occurrence and timing of these events - called cosmic reionizations - are connected with the density, luminosity and spectral hardness of the first photoionizing sources, e.g. stars in galaxies and active galactic nuclei (AGNs). Uncovering when and how these processes took place can therefore provide key information for both the study of the high-redshift IGM and the luminous component of the Universe.

The reionization of H I (and He I) was completed by redshift 6, as evidenced by the lack of Gunn-Peterson absorption troughs in the spectra of high-redshift quasars (e.g. Fan et al. 2006b). It is currently believed that cosmic reionization of He II is delayed to later epochs. This expectation is based on the following arguments: (i) normal star-forming galaxies produce a large amount of photons with energies above 1 ryd - thus ionizing H I - but do not contribute substantially to the cosmic ionizing background above 4 ryd, the ionization threshold of He II; (ii) among all sources with harder spectra, AGNs emit enough radiation to bring He II reionization to completion but their abundance declines much more rapidly than the spatial density of star-forming galaxies at $z > 4$.

Similarly to H I reionization studies, the main observational probes of the final stages of the He reionization process come from the study of the He II Ly α forest in the spectra of high-redshift quasars. Unfortunately, the paucity of the sources for which the far ultraviolet (UV) is not extinguished by intervening H I ab-

* E-mail:

mcompos@astro.uni-bonn.de (MC);

cantal@ucolick.org (SC);

porciani@astro.uni-bonn.de (CP).

sorption and the need to observe from space (given the He II Ly α rest-frame wavelength of 304 Å) resulted to date in a handful of useful lines of sight for He II reionization studies at $2.5 < z < 3.5$ (Syphers et al. 2009; Shull et al. 2010; Worseck & Prochaska 2011; Worseck et al. 2011; Syphers et al. 2012). Since the discovery of the first ‘He II quasar’ Q0302-003, observations with the *Far Ultraviolet Spectroscopic Explorer* (*FUSE*) and the *Cosmic Origins Spectrograph* (*COS*) on the *Hubble Space Telescope* (*HST*) revealed that the mean He II opacity at $z \sim 3$ is much higher than the opacity of H I at similar redshifts (Jakobsen et al. 1994; Syphers et al. 2009; Worseck et al. 2011) with a slow recovery of transmitted flux at $z < 2.7$. While this suggests that He II reionization was indeed completed later than H I reionization, the large scatter and variance between effective He II opacities measured along different sightlines in a wide redshift range indicate that He II reionization may have been a very extended process in time (Syphers et al. 2011a,b; Worseck et al. 2011; Syphers & Shull 2014). The presence of sightlines showing moderate opacity and some transmitted flux at $z \gtrsim 3$ is of particular interest to understand when He II reionization was still ongoing. For $3 < z < 3.5$, typical values for the effective He II optical depth are around 5 (Heap et al. 2000; Zheng et al. 2004; Syphers et al. 2011a; Worseck et al. 2011; Syphers & Shull 2014). Moreover, very recent *COS* observations of 8 new sightlines at $z \sim 3$ and the re-analysis of 11 archival *COS* spectra by Worseck et al. (2014) suggest that the large line-to-line variation and low effective opacities (with optical depths as small as 2) may persist to the highest redshift probed to date, i.e. $z \sim 3.5$. However, these measurements are difficult and require sizable corrections which make them prone to systematic errors. For this reason, no consensus has been reached yet on the transparency of the He II forest at $z > 3.2$ (Syphers, private communication).

The presence of transmitted regions in He II spectra at such a high redshift questions the validity of current models in which He II reionization is triggered by AGN activity only (Worseck et al. 2014). If the high transmissivity of the IGM at $z \sim 3.5$ is confirmed by future studies, it might be necessary to consider the contributions of additional, more exotic, sources in order to reconcile theoretical model and observations. For instance, normal galaxies emit copious soft and hard X-ray photons produced by X-ray binaries (Ranalli et al. 2003; Gilfanov 2004; Mineo et al. 2012; Basu-Zych et al. 2013). The bolometric luminosity of these sources is expected to be several orders of magnitude below the instantaneous luminosity of AGNs, but their time-integrated contribution may be non-negligible, at least in the X-ray band (e.g. Power et al. 2009, 2013; Mirabel et al. 2011; Fragos et al. 2013). However, very little is known about the number of ionizing photons contributed by these sources in the far-UV. Alternatively, shocks due to cosmological structure formation have also been proposed as major contributors to the cosmic UV background above 4 ryd (e.g. Miniati et al. 2004). If these sources are important, He II reionization may have started with very little or no delay with respect to H I reionization. It is worth stressing, however, that, while the bright end of the AGN luminosity function is well constrained by current observations, very little is known about the evolution of the fainter AGNs at $z > 3.5$ (Fontanot et al. 2007; Glikman et al. 2011; Giallongo et al.

2012) and their contribution to the total UV background. Uncertainties in the spectra, opening angle, lifetime and luminosity function make the UV-emissivity of AGNs not well determined. Moreover, yet undetected episodes of black hole accretion that take place in small galaxies at very high redshift (e.g. Ricotti & Ostriker 2004) are not accounted for in the most popular models.

In this paper, we assess the statistical significance with which the data by Worseck et al. (2014), if corroborated by further evidence, would rule out the minimal AGN-based models of He II reionization that have been presented in the literature. These models completely rely on the observed population of AGNs and make very little assumptions. We address this problem using radiative-transfer simulations of AGN-driven He II reionization based on an updated version of the model presented in Compostella et al. (2013, hereafter Paper I). In Paper I, we used high-resolution adaptive mesh refinement (AMR) hydrodynamic simulations to investigate the topology of the He II reionization produced by a population of AGNs that illuminate the computational volumes between $z = 4$ and $z = 2.5$. The initial redshift for the radiative-transfer calculation was chosen to minimize the computational time and some numerical inaccuracies (namely those due to neglecting the hydrodynamic response of the IGM to photoionization, which came out to be much smaller than we originally expected, see appendix A in Paper I and Meiksin & Tittley 2012) given that previous observations and models suggested that He II reionization took place around $z \sim 3$. We showed that the reionization process is highly inhomogeneous and extends for a redshift interval $\Delta z \gtrsim 1$. During this time, the IGM is composed of two phases: sharp ionization fronts expanding around AGNs separate hot regions of completely ionized gas from cold regions where He is still singly ionized. The resulting patchiness of the reionization process gives rise to a bimodal distribution of the IGM temperature and produces two distinct equations of state for the singly ionized and the fully ionized medium.

Mock spectra of the He II Ly α forest extracted from the simulations presented in Paper I were in excellent agreement with low-redshift data. However, for the redshift interval $z > 3.2$ in which data were not available at the time, our model was predicting a rapid increase in the median effective optical depth of small patches in the IGM (see also McQuinn et al. 2009). This fast change was driven by our choice of starting the radiative-transfer calculations at $z = 4$. In fact, early AGNs, although rare, emit enough energetic photons to produce a substantial He III fraction by $z = 4$ (see Fig. 1). In this work, we expand our previous analysis considering the same AGN population used in Paper I but starting now our radiative-transfer computation at much earlier epochs, i.e. $z = 5$ and $z = 6$, with an updated version of our model. In particular, we focus our attention to the evolution of the He II effective optical depth at high redshift and to the direct comparison with the new data that recently became available.

The paper is organized as follows. In Section 2, we describe the numerical simulations adopted in this work and discuss the main properties of the radiative-transfer calculations, focusing on the differences with Paper I. We present the results extracted from mock spectra of the He II Ly α forest in Section 3, where we compare the evolution of the

effective optical depth with the most recent observational data at high redshift. In the same section, we investigate the properties of regions of transmitted flux in He II spectra at high redshift. Finally, we summarize our findings and conclusions in Section 4.

2 METHODS

2.1 Hydrodynamic simulations

We perform a set of hydrodynamic simulations of the IGM with an upgraded version of the publicly available RAMSES code (Teyssier 2002). We adopt a flat Λ cold dark matter cosmology with matter density parameter $\Omega_m = 0.2726$, baryon density parameter $\Omega_b = 0.0456$, and present-day value of the Hubble constant $H_0 = 100 h \text{ km s}^{-1} \text{ Mpc}^{-1}$ with $h = 0.704$. Primordial density perturbations are described by a Gaussian random field with a scale invariant spectrum characterized by the spectral index $n = 0.963$ and a linear rms value within $8 h^{-1} \text{ Mpc}$ spheres of $\sigma_8 = 0.809$. Our assumptions are consistent with results from the *Wilkinson Microwave Anisotropy Probe* presented in Jarosik et al. (2011).

The simulated volume consists of a periodic cubic box $100 h^{-1} \text{ Mpc}$ on a side and is originally discretized into a regular Cartesian mesh with 256^3 elements. We adopt a quasi-Lagrangian AMR strategy based on local density: cells that contain more than eight dark-matter particles (or the proportionate baryonic mass) are tagged for refinement. As a result, six further levels of refinement on top of the base grid are added at $z = 4$ reaching an effective resolution of 16384^3 in the densest regions (corresponding to a cell size of $6 h^{-1} \text{ kpc}$).

We evolve the initial conditions from redshift 120 to 4 assuming that the gas has an ideal equation of state with adiabatic index $\gamma = 5/3$ and a chemical composition produced by big bang nucleosynthesis with a helium mass fraction of 0.24. We neglect small-scale phenomena like star formation, metal enrichment and supernova feedback which have limited impact on the reionization of the intergalactic He.

We model soft UV photons emitted by star-forming regions in galaxies using a spatially uniform, but time-varying, background. We determine the photoionization and photoheating rates of this background by rescaling the model predictions by Haardt & Madau (2012) with a multiplicative factor $C_g(z)$ in order to match the opacity of the IGM measured in observational studies of the H I Ly α forest (see Appendix A for further details).

2.2 Numerical radiative transfer

We study the transmission of hard UV radiation through the IGM by post-processing our hydrodynamic simulations with a modified version of the RADAMESH code (Cantalupo & Porciani 2011): photons emitted by a realistic population of AGNs are propagated through the computational volume allowing for periodic boundary conditions. We sample the spectrum of the sources using 50 frequency bins (10 for H I, 10 for He I and 30 for He II) logarithmically spaced in the energy range $1 - 40 \text{ ryd}$ and we limit the propagation of the ionization fronts to the speed of light.

Run	L_{box} ($h^{-1} \text{ Mpc}$)	ΔL_{min}^a ($h^{-1} \text{ kpc}$)	ΔL_{max}^b ($h^{-1} \text{ kpc}$)	AGN model	z_{AGN}
E1a	100	390	6	PLE	5
E1b	100	390	6	PLE	5
E1c	100	390	6	PLE	5
E2a	100	390	6	PDE	5
E2b	100	390	6	PDE	5
E2c	100	390	6	PDE	5
P1a	100	390	6	PLE	6
P2a	100	390	6	PDE	6

Notes:

^a Size of a resolution element associated with the base grid.

^b Size of a resolution element associated with the highest level of refinement.

Table 1. Summary of the simulations used in this work.

In Paper I, we have shown that neglecting the hydrodynamic response of the gas only generates minor artifacts that do not affect our results in any significant way (see also Meiksin & Tittley 2012).

We use a probabilistic algorithm to populate the simulated dark-matter haloes at $z = 4$ with AGNs (see Paper I for further details). This procedure makes sure that their luminosity function accurately reproduces the measurement by Glikman et al. (2011). The resulting total AGN emissivity at $z = 4$ is roughly 25 per cent higher than in Haardt & Madau (2012). We assume a simple ‘light-bulb’ model, where an AGN shines for 45 Myr with a constant luminosity and then switches off. The spectral energy distribution of the emitted radiation is described by a broken power law with low- and high-frequency indices that are Monte Carlo sampled from the Gaussian distributions given in Vanden Berk et al. (2001) and Telfer et al. (2002), respectively.

We always use the $z = 4$ snapshot of the hydrodynamic simulations to perform the radiative-transfer calculations since the AGN luminosity function by Glikman et al. (2011) has been measured at this redshift. We thus keep the baryonic overdensity $\Delta_b(\mathbf{x}) = \rho_b(\mathbf{x})/\langle\rho_b\rangle$ fixed during the radiative-transfer calculations and scale the mean density $\langle\rho_b\rangle$ proportionally to $(1+z)^3$. Contrary to Paper I, we consider the contribution of an early population of AGNs which turn on at redshift $z_{\text{AGN}} = 5$. Therefore, a choice needs to be made regarding the initial gas temperature and the ionized fractions of H and He to input to RADAMESH. We determine them by enforcing photoionization equilibrium with the UV background at $z = 5$ ¹.

To account for the evolution of the AGN emissivity with time we use the results from Haardt & Madau (2012) (rescaled upwards by 25 per cent to be consistent with the AGN luminosity function at $z = 4$ measured by Glikman et al. 2011) and consider two different approximations. In the Pure Luminosity Evolution (PLE) model, the luminosity of the newly active sources that are associated

¹ The resulting temperature-density relation changes very little between redshifts 5 and 4. For instance, the temperature at mean density decreases by less than 500 K.

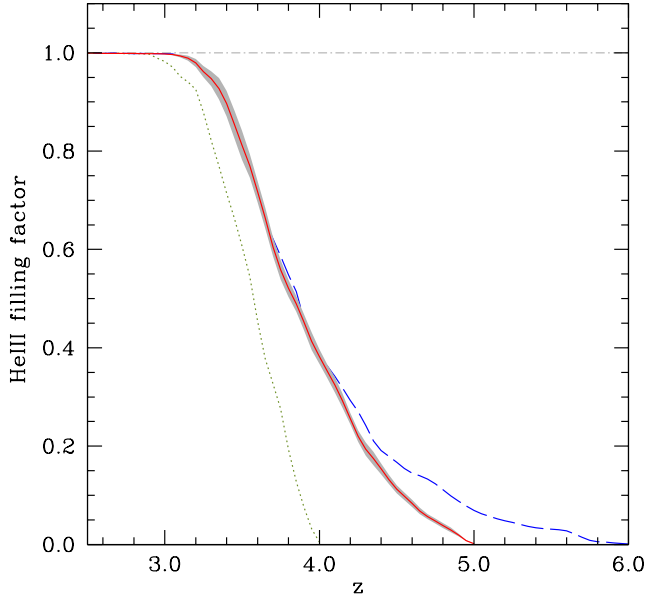


Figure 1. Redshift evolution of the HeIII filling factor in our simulations. The red solid line represents the average in bins of $\delta z = 0.05$ of the simulations with $z_{\text{AGN}} = 5$ presented in this work. The shaded region denotes the standard error of the mean. The blue dashed line indicates the evolution of the mean filling factor in the P simulations. The average of our results from Paper I is also shown for comparison (green dotted line).

with haloes of mass M changes with time, while the total number of active sources in the computational volume scatters around a constant mean value. Conversely, in the Pure Density Evolution (PDE) model, the luminosity of the sources does not evolve with time, while the average number of active sources grows monotonically in the redshift range considered in this work. Further details about both source models are given in Paper I.

We perform three different simulations for each evolutionary model, for a total of six runs. To address the effect of an earlier start of the radiative-transfer calculations, we also perform one run for each source model with $z_{\text{AGN}} = 6$. In Table 1, we summarize the main characteristics of our simulations.

3 RESULTS

In the remainder of this paper, we present the results obtained averaging over all simulations of the E series. In fact, the PLE and PDE runs do not show any systematic difference in the average and scatter of the observables of interest.

3.1 Reionization History

In Fig. 1, we show the evolution of the HeIII filling factor (f_{HeIII} , i.e. the volume-weighted average of the local HeIII fraction) in the E series. At $z = 5$, when we start the radiative-transfer calculations, the abundances of H, He and their ions are set by the soft UV background generated by

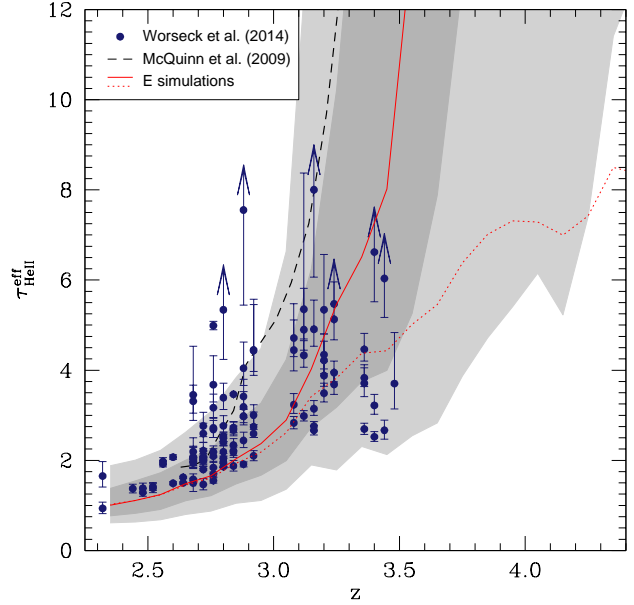


Figure 2. Redshift evolution of the HeII effective optical depth in our simulations using bins of $\Delta z = 0.04$. Shaded areas denote the regions of the $\tau_{\text{HeII}}^{\text{eff}}$ distribution enclosed between the 16th and 84th percentile (dark grey) and between the second and 98th percentile (light grey). The red solid line corresponds to the median value and the red dotted line represents the mean effective optical depth averaged in bins of width $\delta z = 0.1$ to reduce random fluctuations. Observational data by Worbeck et al. (2014) are overplotted for comparison. The black dashed line indicates the median $\tau_{\text{HeII}}^{\text{eff}}$ extracted from the radiative-transfer simulation L3 by McQuinn et al. (2009).

young stars. The initial H I filling factor is $\sim 1 \times 10^{-5}$ and most of the helium is singly ionized. Only 0.1 per cent of the He atoms are either neutral or completely ionized. Turning on an AGN generates an ionization front that rapidly processes and heats the gas elements it crosses. The geometry of the resulting He III region is shaped by the local distribution of matter and reaches a comoving size of several $h^{-1}\text{Mpc}$ before the AGN switches off. At this point, the gas in the ionized bubble cools and the HeIII recombines until new ionization fronts reach the same spatial location. Eventually, different ionization bubbles percolate and progressively fill the entire volume. When the reionization process is concluded, the mean temperature of the gas slowly decreases with time due to Hubble cooling.

At $z = 4$, $f_{\text{HeIII}} \sim 0.38$ and similar values are found also in the simulations of the P series (Fig. 1). This suggests that HeII reionization is a process extended in time which requires an earlier start than assumed in Paper I (where we used $z_{\text{AGN}} = 4$). Note that the E and P series give very similar results for $z < 4$ implying that our findings based on the E simulations should be robust in this redshift range.

The runs with $z_{\text{AGN}} > 4$ show a shallower evolution of f_{HeIII} at early times with respect to Paper I. This is due to the combined action of two effects. First, the integrated quasar emissivity declines at high redshifts. Secondly, the reionization process is more inefficient in a denser

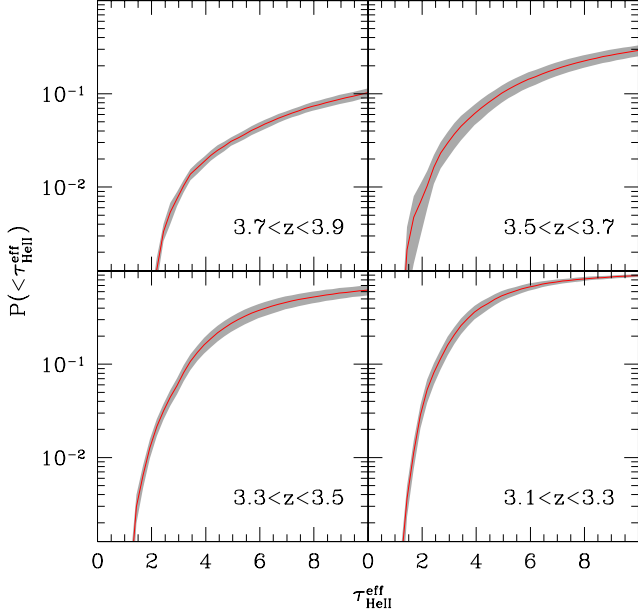


Figure 3. Cumulative distribution of the HeII effective optical depth for different redshift intervals. Solid lines represent the average probability in bins of $\delta\tau_{\text{HeII}}^{\text{eff}} = 0.25$ extracted from our simulations. Shaded regions correspond to the standard error of the mean between the different realizations.

medium because, in the pre-overlap era, individual He III regions quickly recombine when the central source switches off.

The end of the reionization process, defined as the first time He III accounts for 99.5 per cent of the total He content, is achieved at redshift ~ 3 and the He III filling factor increases above 99.9 per cent only at $z < 2.8$. This is in good agreement with the results presented in Paper I, where the late start of the radiative-transfer calculations causes only a slight delay in the completion of the reionization process.

3.2 Effective optical depth

From each simulation, we extract synthetic Ly α absorption spectra considering the distribution and velocity of HeII along 100 sightlines that are parallel to one of the main axes of the box and randomly located in the perpendicular plane. In order to mimic the instrumental response of a real spectrograph, we adopt a resolution element of 1 km s^{-1} and we convolve each spectrum with a Gaussian profile characterized by a kernel with a full width at half-maximum of 88 km s^{-1} . This value corresponds to the nominal resolution of our simulations in the low density regions at $z = 3.5$. Note that our mock spectra are not able to resolve the single absorption features of the Ly α forest, but provide information on the coarse-grained properties of the medium and on the interaction between the sources and the surrounding gas.

We want to compare measurements of the IGM opacity extracted from our spectra against real data from observations of the HeII Ly α forest. For this reason, we evaluate the mean transmitted flux $\bar{F}_i(z)$ ($0 \leq \bar{F}_i(z) \leq 1$) in spectral ‘chunks’ of size $\Delta z = 0.04$ (here the subscript i runs over the

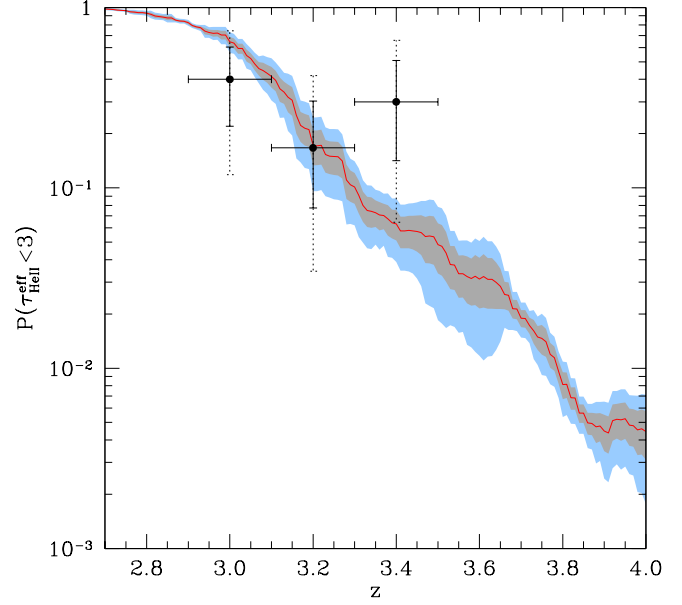


Figure 4. Probability as a function of redshift of measuring $\tau_{\text{HeII}}^{\text{eff}} < 3$ in our simulations. The solid line represents the running average of the different realizations in bins of $\delta z = 0.2$. Shaded regions correspond to 1 (grey) and 2 (cyan) times the standard error of the mean. The probability extracted from observational data by Worseck et al. (2014) together with the two-sided 0.683 (solid) and 0.955 (dotted) confidence level for a binomial distribution are also reported for comparison. Note that the lines do not include the corrective factor for the observability bias. As discussed in Section 3.3.1, this bias will boost the simulated probability by about a factor 1.2 at $z = 3.4$, bringing the simulations in better agreement with the observed fraction of transparent chunks.

different chunks, note that each line of sight includes several of them). We then compute the probability density function of the effective optical depth, $\tau_i^{\text{eff}}(z) = -\ln \bar{F}_i(z)$, considering the chunks (from all simulations) that are contained within a redshift bin of width $\delta z = 0.1$. Finally, we define the mean effective optical depth as $\bar{\tau}_{\text{HeII}}^{\text{eff}}(z) = -\ln(\bar{F}_i(z))_i$ where the mean is taken over the ensemble of chunks that lie within a redshift bin.

In Fig. 2, we compare the distribution of the HeII effective optical depth derived from the E simulations with the observational data points recently presented in Worseck et al. (2014). The shaded regions indicate the range of the simulated $\tau_i^{\text{eff}}(z)$ which is enclosed between the 16th and the 84th percentiles (dark grey) and between the second and the 98th percentiles (light grey). The red solid line shows the median effective optical depth as a function of redshift, while the red dotted line indicates the evolution of mean effective optical depth. For comparison with previous work, we also report the evolution of the median $\tau_{\text{HeII}}^{\text{eff}}(z)$ as predicted by the simulations described in McQuinn et al. (2009), reanalyzed using spectral chunks of size $\Delta z = 0.04$ as in Worseck et al. (2011). Both observations and simulations show large fluctuations in the effective opacity between different lines of sight. Our numerical results are in good agreement with the observational data while the study by McQuinn et al. (2009) predicts too a steep increase in

the effective optical depth with redshift and is therefore unable to match the observed trend. The different AGN luminosity function used by McQuinn et al. (2009) with respect to our study cannot originate this discrepancy. In fact, the evolution in the number density of He II ionizing photons and of the volume averaged He II fraction are very much consistent between the two theoretical models. Although a direct comparison between our radiative-transfer calculation and McQuinn et al. (2009) is complicated by the different algorithms and approximations used, we suspect that the discrepancy is mainly due to the different AGN lifetime models. In particular, McQuinn et al. (2009) use a luminosity-dependent AGN lifetime that decreases with increasing AGN luminosity. As a result, the rarest and brightest AGNs at high redshift are short-lived and therefore produce relatively small He III bubbles. Because the rare, extended regions with low He II opacity at high redshift are typically very highly ionized, they tend to be associated with the proximity regions of the brightest AGNs as we discuss in Section 3.4. The distribution of the simulated $\tau_{\text{He II}}^{\text{eff}}$ at high redshift is very skew and the value of the mean effective optical depth is mostly influenced by these few transmitted regions in He II spectra. Therefore, a model with a luminosity-independent AGN lifetime and larger He III bubbles may be able to produce smaller effective optical depths. We will explore in detail the effects of varying the AGN lifetime model in a future work.

3.3 Statistics

Additional insight into the probability of observing nearly transparent lines of sight at high redshift is provided in Fig. 3, where we show the evolution of the cumulative distribution of the He II effective optical depth in our simulations. Note that this probability is evaluated considering all chunks with $\Delta z = 0.04$ (from all simulations) over redshift bins of size $\delta z = 0.2$. This helps attenuating short-time fluctuations associated with the variation in the number of ionizing photons emitted by the active sources. Shaded regions correspond to the standard error of the mean between the different realizations. At high redshift ($z \sim 3.8$), most of the spectra are completely absorbed and only a small fraction of them shows narrow regions with some transmitted flux. Nearly 10 per cent of the spectra have an effective optical depth smaller than 10 and the probability of detecting lines of sight with $\tau_{\text{He II}}^{\text{eff}} < 2$ is smaller than 1 per mill. As reionization proceeds, the probability of observing regions with transmitted flux increases. Approximately 6 per cent of the sightlines have $\tau_{\text{He II}}^{\text{eff}} < 3$ at $z \sim 3.4$. When He II reionization approaches completion ($3.1 < z < 3.3$, when the He III filling factor is above 0.95) the probability of detecting lines of sight with low opacity further increases: nearly 20 per cent of the sky shows an effective optical depth smaller than 3 while ~ 4 per cent has $\tau_{\text{He II}}^{\text{eff}} < 2$. Finally, at $z \sim 3$, as many as 60–70 per cent of the lines of sight are associated with values of the effective optical depth below 3.

For simplicity, we define as ‘transparent’ a chunk characterized by an effective optical depth $\tau_{\text{He II}}^{\text{eff}} < 3$. On the other hand, we call opaque a chunk in which the effective optical depth is larger than 100. In Fig. 4, we show the probability of measuring a transparent chunk as a function of redshift and directly compare our numerical results with the

z	0.995 CL		0.999 CL		0.9995 CL	
	N_{tr}	N_{tot}	N_{tr}	N_{tot}	N_{tr}	N_{tot}
3.4	5	17	7	23	7	23
3.6	3	10	4	13	5	17
3.8	2	7	3	10	3	10
4.0	2	7	2	7	2	7

Table 2. Number N_{tr} of transparent ($\tau_{\text{He II}}^{\text{eff}} < 3$) and total N_{tot} chunks required at different redshifts to rule out our AGN-driven He II reionization scenario at the 0.995, 0.999 and 0.9995 one-sided Clopper-Pearson confidence levels. It is assumed that the fraction of transparent chunks is $p \sim 0.3$ at all redshifts.

observational data by Worseck et al. (2014). Starting from $z > 2.9$, we consider three redshift bins of size $\delta z = 0.2$ and compute the ratio between the number of transparent and total chunks. The resulting fraction p_{obs} is shown with a solid symbol. If we assume that the different chunks are statistically independent (see Section 3.3.2 for a critical discussion of this working hypothesis), the number of transparent chunks follows a binomial distribution. In this case, p_{obs} is the best estimate for the proportion of transparent chunks in a population, p . In a frequentist sense, confidence intervals for p can be computed using the Clopper-Pearson method (Clopper & Pearson 1934; Gehrels 1986). Error bars in Fig. 4 show the corresponding two-sided 68.3 and 95.5 per cent confidence levels for p .

When reionization is close to completion, simulated data and observations agree well. At higher redshift, the opacity of the IGM in our simulations increases, thus reducing the probability of detecting transparent chunks. This evolution can be noted at $z \sim 3.2$, where observational and simulated data are in excellent agreement suggesting the presence of a higher fraction of He III. However, at the highest redshift probed by observations ($z \sim 3.4$), this trend seems to flatten, while in the simulations the probability decreases monotonically with redshift. Nevertheless, the model predictions lie at the boundary of the 95.67 (two-sided) confidence level for the data (which corresponds to ~ 2 standard deviations, σ , in a Gaussian distribution). Therefore, the model can only be rejected with relatively low statistical significance. Note, however, that it is impossible to determine exact confidence level for a discrete distribution like the binomial one (Neyman 1935) and several studies have shown that the Clopper-Pearson method is too conservative with coverage probabilities that are often higher than their nominal values (e.g. Vollset 1993; Agresti & Coull 1998; Cameron 2011). This implies that the deviation between the data and the model might be more significant than what we found using the Clopper-Pearson method. Alternatively, we perform a Bayesian analysis in the bin at $z \sim 3.4$ and evaluate the posterior distribution of p given the observational data (see the top panel in Fig. 5). We consider two different priors: a flat one and Jeffreys non-informative prior for the binomial distribution. When tested in the frequentist sense, the credibility intervals associated with these posterior distributions provide better coverage probabilities than the Clopper-Pearson method (Cameron 2011). We find that the posterior probability that p is lower than what is predicted by our models is 0.4 and 0.8 per cent for the flat and

N_{tr}	N_{tot}	Clopper-Pearson		Flat prior		Jeffreys prior		Monte Carlo	
		CL	CL _{bias}	CL	CL _{bias}	CL	CL _{bias}	CL	CL _{bias}
3	10	97.840	96.650	99.633	99.334	99.236	98.715	95.601	93.521
6	20	99.886	99.733	99.979	99.942	99.958	99.892	99.490	98.909
9	30	99.993	99.976	99.999	99.995	99.997	99.990	99.932	99.797

Table 3. One-sided frequentist confidence levels and Bayesian credibility levels (per cent) at which our model at $z = 3.4$ is ruled out after observing N_{tot} chunks with $\Delta z = 0.04$ out of which N_{tr} are transparent. Results obtained including the corrective factor for the observability bias are indicated with the subscript ‘bias’.

Jeffreys priors, respectively. In a Gaussian distribution, this corresponds to ~ 2.7 and $\sim 2.4\sigma$ (one-sided) deviations.

In Table 2, we report the number of transparent and total chunks necessary to rule out our AGN-driven He II reionization scenario at the 0.995, 0.999 and 0.9995 (one-sided) Clopper-Pearson confidence levels. For each redshift bin, we select an integer value N_{tr} of transparent chunks and evaluate the corresponding number of total chunks N_{tot} for which the fraction $N_{\text{tr}}/N_{\text{tot}}$ is closest to the value of 0.3 which has been measured at $z \sim 3.4$. We repeat this calculation increasing the number of transparent chunks until the results from our simulations are not anymore compatible with the observational data at the selected confidence level. We find that, at the 0.999 confidence level (corresponding to roughly 3 Gaussian σ) the detection of four additional transparent chunks would be necessary to rule out our reionization model. Observational measurements at $z > 3.4$ would require a smaller amount of lines of sight, but the number of unabsorbed quasars suitable for He II studies drastically decreases. Note that our estimate assumes that $p \sim 0.3$ at all redshifts. If future observations would detect a lower p (as evidenced by our simulations), the values reported in Table 2 are underestimated. In this case, additional transparent chunks from He II quasars would be required to reliably confirm the importance of sources of hard UV photons other than AGNs in the He II reionization.

3.3.1 Observability bias

In the previous analysis we have considered the probability of detecting a transparent chunk from a set of randomly drawn lines of sight in our simulation boxes and compared it to observations. In reality, however, the selection of observed lines of sight is not random: any intervening, optically thick H I system may extinguish the quasar continuum at or below the He II edge, rendering the He II opacity measurements impossible. Indeed, because of the accumulated absorption by H I systems in the spectra of $z > 3$ quasars, only a few per cent of them - the so-called He II quasars - are suitable targets for He II studies (see e.g. Worseck & Prochaska 2011). The vast majority of intervening systems are at much lower redshift than the regions probed by the He II spectra. However, the He II quasar selection technique also rejects targets with H I absorbers at $z > 3$ that are thick enough to extinguish the quasar far-UV flux (Worseck & Prochaska 2011). For instance, considering a spectral chunk at $z = 3.4$, all lines of sight containing a Lyman limit system (LLS) with $\tau_{\text{H I}}^{\text{eff}} > 5$ at the same redshift will be extinguished at the He II edge and therefore not included in the observed sample. This introduces an *observability bias* that is redshift de-

pendent and that is not included in the randomly selected sample of lines of sight in our simulations. Clearly, the effect of the observability bias is to remove He II opaque lines of sight from the sample and therefore boost the fraction of transparent chunks with respect to a randomly selected sample. How important is this effect? Unfortunately, current large cosmological simulations cannot directly resolve the LLSs, and this is especially true for our simulations that are aimed for volume rather than resolution. Therefore, we cannot directly reproduce the observability bias with our simulations. However, we can estimate the fraction f_{LLS} of lines of sight in our computational boxes that should contain a LLS with $\tau_{\text{H I}} > 5$ [or $\log(N_{\text{H I}}/\text{cm}^{-2}) > 17.9$] using the observed differential number density of LLSs as a function of redshift (Prochaska et al. 2010; Songaila & Cowie 2010). We then rank our n_{tot} simulated lines of sight by their total $N_{\text{H I}}$ in decreasing order and remove from our sample the first $f_{\text{LLS}} \times n_{\text{tot}}$, with the very plausible assumption that the lines of sight with the highest column density would be associated with LLSs at higher resolution. Once we make this correction, we obtain a fraction of simulated transparent chunks at $z \sim 3.4$ that is a factor 1.2 higher than for randomly selected lines of sight, further relieving the tension between the model and the observations. In fact, the predictions of our simulations now lie within the 93.3 per cent (two-sided) Clopper-Pearson confidence level (corresponding to $\sim 1.8\sigma$ in the Gaussian case). On the other hand, the Bayesian posterior probability grows to 0.7 and 1.3 per cent (i.e. ~ 2.5 and $\sim 2.2\sigma$ for the Gaussian statistics). Note that this factor is not included in the model lines presented in Fig. 4.

3.3.2 Accounting for statistical correlations

The 10 chunks observed at $z \sim 3.4$ are extracted from four quasar spectra and the transparent ones come from only two lines of sight (Worseck et al. 2014). This suggests that the assumption of statistical independence between the chunks is likely to be violated so that the binomial distribution does not apply. In order to quantify the importance of this effect, we use a Monte Carlo method to resample four random lines of sight from our simulations and extract 10 chunks out of them with the same pattern (i.e. number of considered chunks per observed sightline) as in Worseck et al. (2014). The resulting cumulative probability distribution is shown in the bottom panel of Fig. 5. While there is a considerable probability of detecting a number of transparent chunks equal to or higher than one or two (47.6 and 17.0 per cent, respectively), the chance of matching the observational data ($n_{\text{tr}} \geq 3$) is of 4.4 per cent. This corresponds to

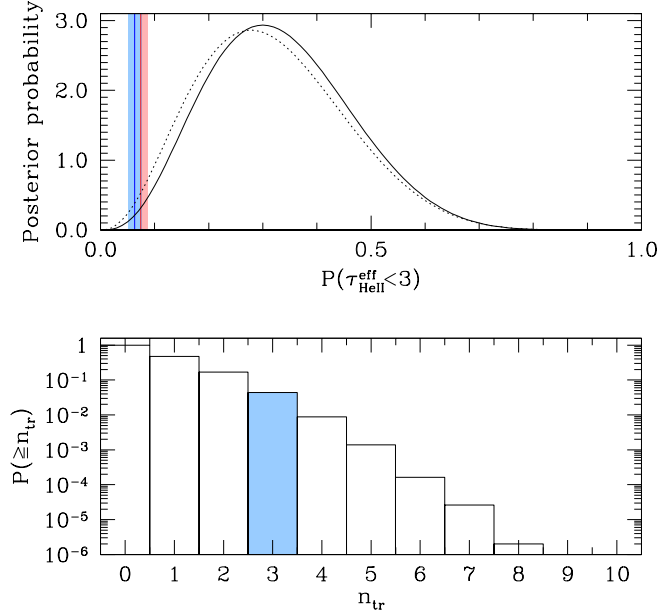


Figure 5. Top: posterior probability distribution for the fraction of transparent chunks given the observational data in the redshift bin at $z \sim 3.4$. The solid curve assumes a flat prior, while the dotted curve corresponds to Jeffreys non-informative prior. Vertical lines indicate the results extracted from our numerical simulations without accounting for observability bias (blue) and using the corrective factor discussed in Section 3.3.1 (red). Shaded regions denote the 1σ uncertainty of our model. Bottom: probability of detecting n_{tr} or more transparent chunks within 10 chunks selected as in Worseck et al. (2014) in the redshift bin $3.3 < z < 3.5$. The value of $n_{\text{tr}} = 3$ observed with four lines of sight by Worseck et al. (2014) occurs with a probability of 4.4 per cent in our simulations (shaded area).

the probability above 1.7σ in a Gaussian distribution, showing that correlations among the data make the deviation of our model less statistically significant than what is found using the binomial approximation². Replicating this analysis while accounting for the observability bias, the probability of matching the observational data increases to 6.5 per cent or, equivalently, 1.5σ in a Gaussian distribution. In Table 3, we report the one-sided confidence levels and credibility levels at which our model of HeII reionization is ruled out according to the different statistical methods considered in this work. We select integer multiples of the number of transparent and total chunks obtained from observations at $z \sim 3.4$ and evaluate the confidence levels between these data and the results from our simulations for the Clopper-Pearson analysis, the Bayesian analysis (both with flat and Jeffreys priors) and the Monte Carlo analysis. In the last case, the chunks in the lines of sight are selected duplicating the observed pattern, as previously discussed. For each method we include the results obtained considering the corrective factor

² We have checked that considering one chunk per sightline in our simulations perfectly reproduces the binomial predictions showing that the finite size of the simulation box does not introduce any detectable correlations.

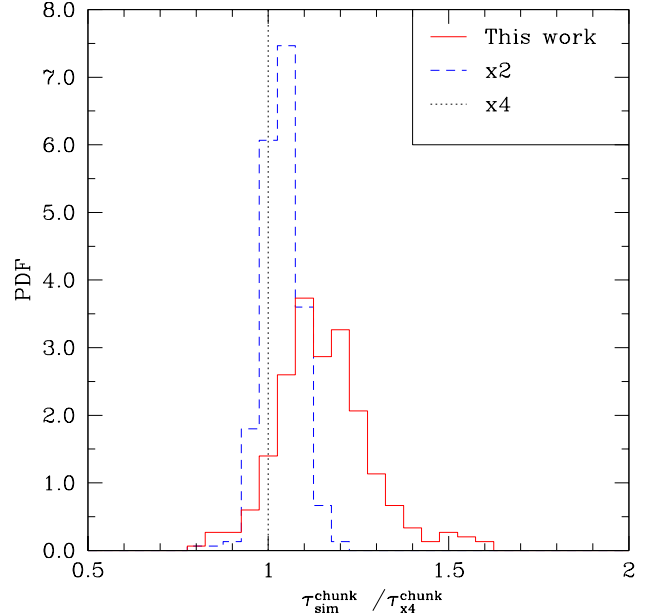


Figure 6. Quantification of resolution effects on the measurement of $\tau_{\text{HeII}}^{\text{eff}}$ (measured in bins of $\Delta z = 0.04$ at $z = 3.4$) in numerical simulations. We consider three AMR simulations in which the same realization of the IGM is evolved using resolution elements with different sizes for the base grid (see main text for details). We consider the same resolution used for our study of helium reionization (red solid) and two other resolution elements whose linear size is a factor of 2 (blue dashed) and 4 (black dotted) smaller. Plotted is the PDF of the ratio between $\tau_{\text{HeII}}^{\text{eff}}$ evaluated for the same chunk at a given resolution and at the maximum resolution.

Method	CL	σ	CL _{bias}	σ_{bias}
Clopper-Pearson	91.14	1.35	87.63	1.16
Flat prior	97.44	1.95	95.91	1.74
Jeffreys prior	95.84	1.73	93.75	1.53
Monte Carlo	86.67	1.11	82.25	0.93

Table 4. One-sided frequentist confidence levels and Bayesian credibility levels (per cent and equivalent number of Gaussian standard deviations) at which our model at $z = 3.4$ is ruled out by the observational data in Worseck et al. (2014) after accounting for finite-resolution effects in our simulations. Results obtained including the corrective factor for the observability bias are indicated with the subscript ‘bias’.

for the observability bias (indicated by the subscript ‘bias’). Based on this study, we conclude that the tension between the observational data and the AGN-driven scenario of HeII reionization is mild and additional data are required to rule out the model with a convincing statistical significance.

3.3.3 Numerical resolution effects

The HeII Ly α transition has a large cross-section (relative to hydrogen) and transmission through the IGM is primarily associated with low-density gas (see e.g Rauch 1998). Due to their finite spatial resolution, numerical simulations tend

to overestimate the density in these regions and to overpredict the corresponding He II effective optical depth (see e.g. Theuns et al. 1998, for a discussion of this effect in smoothed particle hydrodynamic simulations). In order to account for systematic errors, we study how $\tau_{\text{He II}}^{\text{eff}}$ at $z = 3.4$ varies with the resolution of the base grid of our AMR simulations. We start from the base mesh given in Table 1 and we decrease the linear size of the resolution element by a factor of 2 and 4. We process these three boxes with the RADAMESH code and extract spectra of the He II Ly α forest in redshift bins of $\Delta z = 0.04$ probing exactly the same density field at different resolutions. As a source of ionizing radiation we use a uniform background whose amplitude is fixed to reproduce the mean transmissivity³ found in the simulations with radiative transfer discussed above. A convergence study is provided in Fig. 6, where we show the probability distribution function of the ratio between the effective optical depths evaluated, for the same chunk, in a given simulation and in the simulation with the highest resolution. This test suggests that the simulations with radiative transfer adopted in this work might overestimate the He II optical depth by about 15 per cent on average. Therefore resolution effects should further alleviate the tension between our simulations and the observational data at $z \sim 3.4$. We approximately quantify their impact by convolving the PDF of $\tau_{\text{He II}}^{\text{eff}}$ determined in Section 3.2 with the correction given in Fig. 6. The corresponding frequentist confidence levels and the Bayesian credibility levels at which our model is ruled out are reported in Table 4 for the different statistical methods considered in this work, where the subscript ‘bias’ indicates the values obtained considering the corrective factor for the observability bias. We conclude that the discrepancy between the observational data by Worseck et al. (2014) and our simulations is only a 1σ to 2σ effect.

3.4 The nature of transmitted chunks at $z = 3.4$

The opacity at 304 \AA of a gas element is directly related to the fraction of He II in the cell which, in turn, can be linked to the interplay between the density (governing the rate of recombinations), the local flux of ionizing photons (responsible for the rate of photoionizations) and the temperature of the gas. In Fig. 7, we compare the properties of transmitted and opaque chunks extracted from our mock spectra in the redshift interval $3.3 < z < 3.5$. We associate to each transparent chunk a representative cell that corresponds to the maximum transmitted flux in the chunk (circles), while a random cell within the chunk is associated to each opaque region of the spectrum (crosses). The scatter plot presents the relationship between the photoionization rate $\Gamma_{\text{He II}}$ and the baryonic overdensity Δ_b and is colour-coded with respect to the temperature T of the gas element. Cells associated with transparent chunks are predominantly located in mean or underdense regions (mainly because of the selection criterion) and show a large spread in the values of the temperature. The photoionization rate is systematically larger than what is observed for opaque chunks. These completely absorbed regions extend to higher density and are

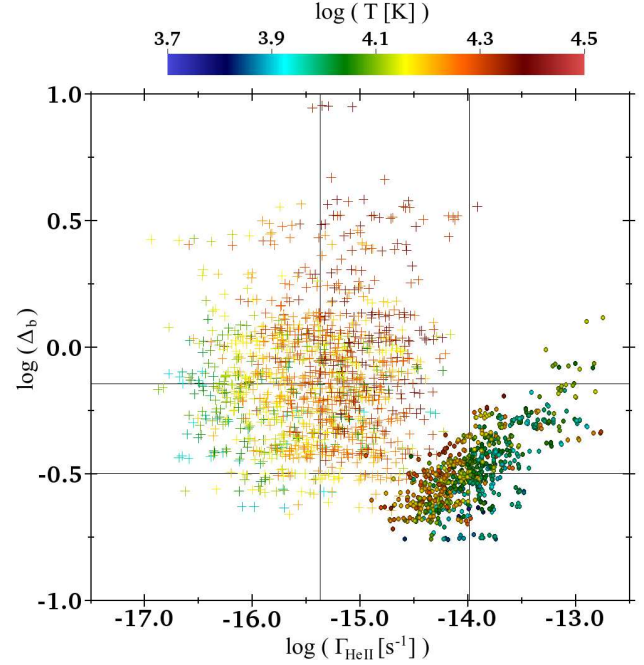


Figure 7. Distribution of the helium photoionization rate $\Gamma_{\text{He II}}$ and the baryonic overdensity Δ_b for gas elements associated with transparent (circles) and opaque (crosses) chunks of size $\Delta z = 0.04$ in the redshift interval $3.3 < z < 3.5$. Points are colour-coded based on the logarithm of the gas temperature as indicated by the colour bar. Solid lines indicate the median values of the distributions.

described by an average temperature that is to some extent higher with respect to the transmitted case.

In order to evaluate the origin of the transparent regions in He II spectra, we can associate to each representative cell the source that contributes the most to the local $\Gamma_{\text{He II}}$. The average distance between this source and the representative cell is generally smaller ($\sim 13.6 h^{-1} \text{Mpc}$ comoving) for transparent chunks with respect to the value observed for opaque regions ($\sim 17.2 h^{-1} \text{Mpc}$) or for a random distribution of points in the computational box ($\sim 16.3 h^{-1} \text{Mpc}$). In roughly half of the transparent (57 per cent) and opaque (49 per cent) chunks, the fraction of the total ionizing flux supplied by this single AGN is higher than 90 per cent. Although one source generally provides the main contribution, cells associated with transparent chunks often receive photons from several different AGNs located nearby, thus being characterized by a large total photoionization rate ($\Gamma_{\text{He II}} > 10^{-15} \text{ s}^{-1}$ for all cells associated with transparent chunks). On the other hand, opaque chunks are generally affected by one single source and only a small fraction of them receive a significant number of ionizing photons. On the grounds of this evidence, we can infer that regions of transmitted flux in He II Ly α spectra at high redshift can be originated by two different effects. The first possibility arises when the line of sight crosses the proximity region (i.e. the zone in which the ionizing flux due to the dominant source is larger than the contribution due to all other AGNs) of a single luminous AGN. In this case, the large photoionization rate within the ionization front produces transparent chunks that can be ascribed to the so-called ‘transverse proximity effect’. A

³ Note that a uniform radiation field produces less optically thick regions than a set of discrete sources.

second, less common, possibility occurs when the transmitting region is close to several, fainter, AGNs. In this case the combined photoionization rate produced by the sources is strong enough to generate a transparent chunk.

4 CONCLUSIONS

We perform hydrodynamic simulations of the epoch of He II reionization adopting the same technique presented in Paper I: the output of an AMR run is post-processed using a modified version of the radiative-transfer code RADAMESH (Cantalupo & Porciani 2011). We use the quasar luminosity function observed in the redshift range $3.5 < z < 5.2$ to calibrate the magnitude of the sources in our simulated volumes, producing a realistic population of AGNs that turn on at $z_{\text{AGN}} = 5$. We consider different models for the redshift evolution of the emissivity of the sources and perform several runs to account for the different ionization history associated with the position and luminosity of the AGNs. We extract simulated spectra of the He II Ly α forest from our computational volumes and compare our results with the most recent observational data available to date (Worseck et al. 2014).

In agreement with our previous theoretical work and with observations of the intergalactic He II absorption in *HST/COS* spectra, we find that the observed quasar population can completely ionize most of the He in the IGM by $z \sim 3$. All computational volumes show that the He II fraction drops below 0.5 per cent in the redshift interval $2.9 \leq z \leq 3.1$, with a He III filling factor larger than 99.9 per cent for $z < 2.8$. The completion of the reionization seems to be unaffected by the exact start of the radiative-transfer calculations as long as a sufficiently extended reionization process is considered. However, the increasing gas density and the decline of the AGN abundance towards high redshifts cause a slower evolution of the IGM properties during the early stages of He II reionization with respect to the results of Paper I.

The effective optical depth of the He II Ly α forest extracted from simulated spectra matches the observational data by Worseck et al. (2014) at all redshifts. Additional sources of hard UV photons beyond AGNs are not required to explain current data. However, moderate tension (at about the Gaussian 2σ level) is present at the highest redshift which has been currently probed by observations ($z \sim 3.4$). Accounting for resolution effects in our simulations further alleviates the tension with the observational data (the significance of the discrepancy drops between 1σ and 2σ depending on the statistical method adopted).

For $z > 3$, our model predicts a large variability between different lines of sight generated by the ongoing reionization process as found by observations. At these redshifts, $\tau_{\text{He II}}^{\text{eff}}$ evaluated in chunks of $\Delta z = 0.04$ has a very broad and skew distribution. The median effective optical depth increases at high redshifts more slowly than previous numerical simulations (e.g. McQuinn et al. 2009), accounting for small, but rare, values of $\tau_{\text{He II}}^{\text{eff}}$ up to $z \sim 4$. The fluctuations in the effective optical depth predicted by our model correlate with large variations in the temperature of the medium that persist after the completion of the reionization process.

Transparent lines of sight at high redshifts are generated by the joint influence of the density, the temperature

and, mostly, the local photoionization rate. Regions of high transmissivity in He II spectra are usually underdense and cross the proximity regions of luminous sources capitalizing on the transverse proximity effect generated by bright AGNs. In other cases, the transmitted region is generated by the contribution of several, less luminous, sources that provide the required number of ionizing photons. During the final phases of He reionization, the temperature of these transparent regions is generally slightly lower than what is measured for regions of high opacity. This reflects the fact that transparent regions have been ionized earlier and are characterized by a He II fraction of $f_{\text{He II}} \sim 10^{-3}$ or lower, while opaque regions are still experiencing ionization.

The moderate tension between the simulated and observed $\tau_{\text{He II}}^{\text{eff}}$ may be due to the observability bias, a systematic lack of UV photons in the models (associated with the poorly constrained shape of the AGN luminosity function, lifetime and spectral energy distribution at high redshift), or, simply, a statistical fluctuation in the observational data. In order to rule out our model with high significance, the sample size at $z \sim 3.4$ needs to be at least two or three times bigger than it is now. If future data will confirm the current measurements, there will be sufficient evidence for considering additional hard UV radiation and, maybe, other sources beyond AGNs.

A key challenge in a complete characterization of the reionization process remains: constraining the evolution of the He II effective optical depth at redshift $z \geq 3.5$. When a sufficient number of lines of sight towards He II quasars will become available in the future, tighter constraints on the timing, topology and the sources of He II reionization will be placed from the joint analysis of simulated and observed transparent lines of sight.

ACKNOWLEDGEMENTS

We thank an anonymous referee for helpful comments which improved the quality of this work. MC thanks Gabor Worseck for providing the observational data before publication and David Syphers for his constructive comments and suggestions on an earlier version of the paper. Numerical simulations were run at the Leibniz-Rechenzentrum centre in Munich. This work is carried out within the Collaborative Research Centre 956, sub-project C4, funded by the Deutsche Forschungsgemeinschaft (DFG). SC acknowledges support from the NSF AST-1010004 and STScI HST GO-13013.04-A grants.

References

- Agresti, A., Coull, B. A. 1998, *The American Statistician*, 52, 2, 119
- Basu-Zych, A. R., Lehmer, B. D., Hornschemeier, A. E., et al. 2013, *ApJ*, 774, 152
- Becker, G. D., Hewett, P. C., Worseck, G., & Prochaska, J. X. 2013, *MNRAS*, 430, 2067
- Cameron, E. 2011, *PASA*, 28, 128
- Cantalupo, S., & Porciani, C. 2011, *MNRAS*, 411, 1678
- Clopper, C. J., & Pearson, E. S. 1934, *Biometrika*, 26, 404

Compostella, M., Cantalupo, S., & Porciani, C. 2013, MNRAS, 435, 3169

Croft, R. A. C., Weinberg, D. H., Katz, N., & Hernquist, L. 1998, ApJ, 495, 44

Fan, X., Carilli, C. L., & Keating, B. 2006a, ARA&A, 44, 415

Fan, X., Strauss, M. A., Becker, R. H., et al. 2006b, AJ, 132, 117

Fontanot, F., Cristiani, S., Monaco, P., et al. 2007, A&A, 461, 39

Fragos, T., Lehmer, B., Tremmel, M., et al. 2013, ApJ, 764, 41

Gehrels, N. 1986, ApJ, 303, 336

Giallongo, E., Menci, N., Fiore, F., et al. 2012, ApJ, 755, 124

Gilfanov, M. 2004, MNRAS, 349, 146

Glikman, E., Djorgovski, S. G., Stern, D., et al. 2011, ApJL, 728, L26

Haardt, F., & Madau, P. 2012, ApJ, 746, 125

Heap, S. R., Williger, G. M., Smette, A., et al. 2000, ApJ, 534, 69

Jakobsen, P., Boksenberg, A., Deharveng, J. M., et al. 1994, Nature, 370, 35

Jarosik, N., Bennett, C. L., Dunkley, J., et al. 2011, ApJS, 192, 14

McQuinn, M., Lidz, A., Zaldarriaga, M., et al. 2009, ApJ, 694, 842

Meiksin, A. A. 2009, Reviews of Modern Physics, 81, 1405

Meiksin, A., & Tittley, E. R. 2012, MNRAS, 423, 7

Mineo, S., Gilfanov, M., & Sunyaev, R. 2012, MNRAS, 419, 2095

Miniati, F., Ferrara, A., White, S. D. M., & Bianchi, S. 2004, MNRAS, 348, 964

Mirabel, I. F., Dijkstra, M., Laurent, P., Loeb, A., & Pritchard, J. R. 2011, A&A, 528, A149

Neyman, J. 1935, The Annals of Mathematical Statistics, 6, 111

Power, C., Wynn, G. A., Combet, C., & Wilkinson, M. I. 2009, MNRAS, 395, 1146

Power, C., James, G., Combet, C., & Wynn, G. 2013, ApJ, 764, 76

Prochaska, J. X., O'Meara, J. M., & Worseck, G. 2010, ApJ, 718, 392

Ranalli, P., Comastri, A., & Setti, G. 2003, A&A, 399, 39

Rauch, M. 1998, ARA&A, 36, 267

Ricotti, M., & Ostriker, J. P. 2004, MNRAS, 352, 547

Shull, J. M., France, K., Danforth, C. W., Smith, B., & Tumlinson, J. 2010, ApJ, 722, 1312

Songaila, A., & Cowie, L. L. 2010, ApJ, 721, 1448

Syphers, D., Anderson, S. F., Zheng, W., et al. 2009, ApJ, 690, 1181

Syphers, D., Anderson, S. F., Zheng, W., et al. 2011a, ApJ, 726, 111

Syphers, D., Anderson, S. F., Zheng, W., et al. 2011b, ApJ, 742, 99

Syphers, D., Anderson, S. F., Zheng, W., et al. 2012, AJ, 143, 100

Syphers, D., & Shull, J. M. 2014, ApJ, 784, 42

Telfer, R. C., Zheng, W., Kriss, G. A., & Davidsen, A. F. 2002, ApJ, 565, 773

Teyssier, R. 2002, A&A, 385, 337

Theuns, T., Leonard, A., Efstathiou, G., Pearce, F. R., &

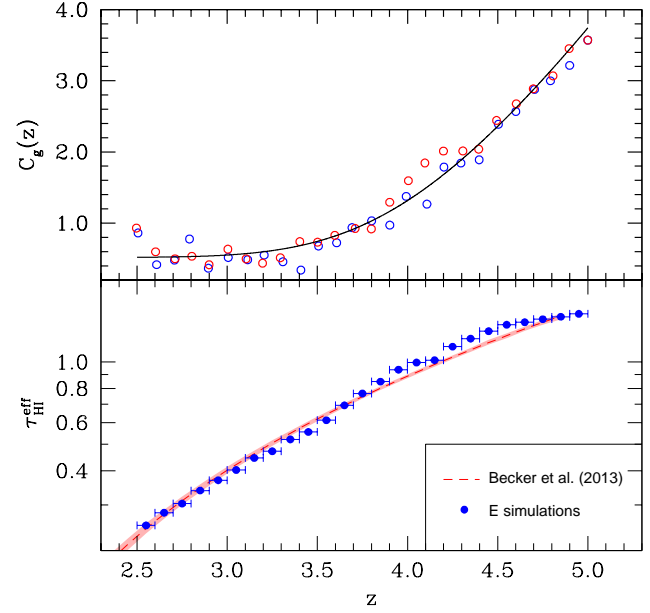


Figure A1. Top: redshift evolution of the multiplicative correction factor $C_g(z)$. Circles represent the value of $C_g(z)$ that must be applied to two test simulations (PLE in blue and PDE in red) in order to match observations of the H I effective optical depth. The solid line represents the fit given in equation (A1). Bottom: redshift evolution of the H I effective optical depth in our simulations evaluated using bins of $\Delta z = 0.1$. The analytic fit to observational data (red dashed line) by Becker et al. (2013) and its 1σ uncertainty (shaded region) are also reported for comparison.

Thomas, P. A. 1998, MNRAS, 301, 478

Vanden Berk, D. E., Richards, G. T., Bauer, A., et al. 2001, AJ, 122, 549

Vollset, S. E. 1993, Statistics in Medicine, 12, 809-824

Worseck, G., & Prochaska, J. X. 2011, ApJ, 728, 23

Worseck, G., Prochaska, J. X., McQuinn, M., et al. 2011, ApJL, 733, L24

Worseck, G., Prochaska, J. X., Hennawi, J. F., & McQuinn, M. 2014, arXiv:1405.7405

Zheng, W., Chiu, K., Anderson, S. F., et al. 2004, AJ, 127, 656

APPENDIX A: SOFT UV BACKGROUND

Our simulations use the soft UV background computed by Haardt & Madau (2012) as a template. Assuming that the temperature of the IGM is 20 000 K, this model reproduces the observed evolution of the effective optical depth in the H I Ly α line (Haardt & Madau 2012). However, most of the gas in our simulations never becomes so hot. For instance, the average gas temperature at mean density is of approximately 6500 K at $z = 5$ and does not exceed 17 000 K even when it reaches its peak value during He II reionization at $z \sim 3.4$. Since the H I opacity strongly depends on the temperature of the absorbing gas, we need to use a different UV background to match the observed evolution of

the IGM transmissivity. One possibility would be to leave the photoionization rate unchanged and increase the photoheating rate. However, this would require the presence of much harder sources of radiation which are difficult to reconcile with the assumption that only young stars contribute at early times. We therefore prefer to rescale the predictions by Haardt & Madau (2012) with a redshift-dependent multiplicative factor, $C_g(z)$, which is determined requiring that the H I transmissivity of the Ly α forest reproduces the most recent observational measurements by Becker et al. (2013). To estimate the amplitude of the correction factor, we run two radiative-transfer simulations of He II reionization using the soft UV background computed by Haardt & Madau (2012) combined with our two source models for AGNs (PLE or PDE). We then use the fluctuating Gunn-Peterson approximation (Croft et al. 1998) to scale the IGM opacity in the simulations in order to match the data by Becker et al. (2013). We find that the expression

$$C_g(z) = 0.26 [\tanh(z - 3.8) + 1] (z - 2.4)^2 + 0.52 \quad (\text{A1})$$

provides a good analytical approximation to the numerical results (see the top panel in Fig. A1).

As a cross check, the bottom panel in Fig. A1 shows that the H I effective optical depth extracted from our simulations matches the observational data points basically at all times. Note, however, that the opacity extracted from the mock spectra is very sensitive to random fluctuations in the number and luminosity of the ionizing sources. For instance, the slight excess of opacity seen at $z \sim 4.4$ must be ascribed to a temporary decrease in the number of ionizing photons emitted within the computational volumes per unit time.

This paper has been typeset from a \LaTeX file prepared by the author.